First in situ measurements of the prototype Tesseract fluxgate magnetometer on the ACES-II-Low sounding rocket

Kenton Greene[1], Scott R. Bounds[1], Robert M. Broadfoot[1], Connor Feltman[1], Samuel J. Hisel[1], Ryan M. Kraus[2], Amanda Lasko[1], Antonio Washington[1], and David M. Miles[1]

[1]Department of Physics and Astronomy, University of Iowa, Iowa City, IA, USA
[2]Peraton, NASA Sounding Rockets Operations Contract, Wallops Island, VA, USA

Correspondence: Kenton Greene (kenton-greene@uiowa.edu)

Abstract. Ongoing innovation in next-generation fluxgate magnetometry is important for enabling future investigations of space plasma, especially multi-spacecraft experimental studies of energy transport in the magnetosphere and the solar wind. Demonstrating the spaceflight capability of novel designs is an important step in the instrument development process; however, large-scale satellite missions are often unwilling to accept the risks of an instrument without flight heritage. The Tesseract – a novel fluxgate magnetometer sensor design – had an opportunity for an inaugural spaceflight demonstration on the ACES-II sounding rocket mission, which launched from Andøya Space Center in Andenes, Norway, in November 2022. Tesseract's design takes advantage of a new racetrack core geometry to create a sensor that addresses some of the issues that contribute to instability in more traditional ring-core designs. Here we present the design of a prototype fluxgate magnetometer based on the new Tesseract sensor, its pre-flight characteristics, and an evaluation of its in-flight performance aboard ACES-II. We find that the magnetic field measured by Tesseract over the course of the flight was in strong agreement with both the onboard ACES II reference ring-core fluxgate magnetometer and the predictions of a geomagnetic field model. The Tesseract-based magnetometer measured signatures of field-aligned currents and potential Alfvén wave activity as it crossed an active auroral arc, and we conclude that it performed as expected. Tesseract will be flown on the Tandem Reconnection and Cusp Electrodynamics Reconnaissance Satellites (TRACERS) Small Explorers (SMEX) satellite mission as part of the MAGnetometers for Innovation and Capability (MAGIC) technology demonstration currently scheduled to launch in 2025.

1 Introduction

Fluxgate magnetometers are important tools for spaceborne investigations of space plasma processes that are responsible for transporting energy and mass throughout the coupled solar–terrestrial system. Continued innovation in reliable, precise fluxgate magnetometer technology is important for enabling the next generation of space plasma science missions, especially multi-spacecraft investigations of magnetosphere and solar wind plasma. Recent multi-spacecraft missions, such as Swarm (Merayo et al., 2008), the Magnetospheric Multiscale Mission (MMS) (Russell et al., 2016), Space Technology 5 (ST-5) (Slavin et al., 2008), Themis (Auster et al., 2008), and Cluster (Balogh et al., 1997), have made important breakthroughs in our understanding of the multiscale plasma waves and current structures that drive the dynamic exchange of energy between the magnetosphere and ionosphere. For example, recent statistical studies of the morphology of terrestrial field-aligned current systems (i.e., Gjerloev et al., 2011; Lühr et al., 2015; Pakhotin et al., 2020; Cheng et al., 2021) depend on stable multipoint fluxgate measurements from missions like Cluster, Swarm, and ST-5 to reliably resolve the small spatiotemporal magnetic fluctuations that enable precise monitoring of magnetospheric energy flux over variations in solar wind conditions. High-stability, low-noise multi-spacecraft fluxgate measurements have also made important contributions to our understanding

of interplanetary plasma. For example, statistical studies of solar wind plasma, using fluxgate magnetometer data from MMS with a $8\,\mathrm{nT}\,(\mathrm{Hz})^{(-1/2)}$ instrumental noise floor in the low field range (Russell et al., 2016), were able to resolve proton and electron inertial-scale turbulence that plays an important role in the heating and dissipation of solar wind and magnetosheath plasma (Chhiber et al., 2018; Chasapis et al., 2020). Recent multi-spacecraft missions have increasingly focused on flying three-axis compensated fluxgate sensors in the interest of maximizing instrumental stability. However, three-axis compensated sensor designs that have flown on these past missions have all been limited to accommodate some variation of the traditional spiral-wound ring-geometry ferromagnetic core (e.g., Acuña et al., 1978).

New advances in fluxgate core technology (Miles et al., 2022; Narod and Miles, 2024) are enabling new designs for fluxgate sensors not previously possible with ring cores. Miles et al. (2019) enabled the manufacturing of new miniature racetrack geometry cores which were found to have a more consistent yield and lower-noise-performance cores than the traditional ring-core manufacturing process (Miles et al., 2022). Greene et al. (2022) developed a new Tesseract sensor design capable of accommodating this new racetrack core geometry, while simultaneously addressing some of the design issues that are thought to cause instability in the more traditional ring-core design (i.e., Acuna et al., 1978; Wallis et al., 2015). Preliminary testing (Greene et al., 2022) found that the Tesseract sensor performs very well in metrics that are associated with instrumental stability and low noise and concluded that the sensor design looks promising for making low-noise, stable magnetic measurements in a magnetospheric environment.

However, obtaining space flight heritage for new instrument designs is notoriously difficult. Large-scale missions like those described above are typically unwilling to accept the risks associated with an instrument that does not have demonstrated flight heritage. Sounding rockets are an excellent low-cost, low-consequence alternative for new instrument designs in need of an opportunity to demonstrate space flight capability.

The Tesseract fluxgate instrument was offered a flight opportunity on the ACES-II sounding rocket as a ride-along technology demonstration. ACES-II was a sounding rocket mission that used a high- and low-flyer pair to study the auroral electrical current systems that are a key energy transport mechanism between the magnetosphere and the ionosphere. A Tesseract-based fluxgate magnetometer prototype was launched aboard the ACES II low-flyer sounding rocket from the Andøya Space Rocket Range in Andenes, Norway, on 20 November 2022 at 17:21:40 UTC. The two-stage Black Brant XI rocket reached apogee at an altitude of 188 km as it intercepted an active, discrete auroral arc. In this paper, we describe the design and construction of a prototype fluxgate magnetometer based on the Tesseract sensor design and

present its in situ measurements of magnetic perturbations associated with auroral electrodynamics.

2   The new Tesseract-based magnetometer design

Fluxgate magnetometers (Primdahl, 1979) measure the static and low-frequency magnetic field by modulating the local magnetic flux and measuring the resulting electromotive force induced in a sense winding. A ferromagnetic core is periodically driven into magnetic saturation at frequency f. This effectively gates the local magnetic field, thereby inducing a $2f$ signal due to the nonlinear magnetic permeability of the core as it enters magnetic saturation. The amplitude of this $2f$ signal is equal to the background magnetic field times a scale factor S. Two or more cores and windings, arranged orthogonally to one another, allow for the measurement of the full vector magnetic field.

The fidelity of a fluxgate's magnetic field measurement varies over time when its calibration parameters, sensitivity S, orthogonality A, and offset O, vary with changes in temperature or over time. For example, the alignment of a fluxgate's three orthogonal axes, described by A, has been known to vary due to thermal and mechanical strain on the sensor (Primdahl, 1979). Many spaceborne fluxgates, including the Tesseract, use global negative magnetic feedback to null the magnetic field inside the sensor, which linearizes and extends the measurement range of the instrument (Primdahl and Jensen, 1982). An inhomogeneous or inconsistent magnetic null is thought to contribute to instability of a fluxgate's instrumental offset (Ripka, 1992), orthogonality (Petrucha et al., 2015), and sensitivity (Korepanov and Marusenkov, 2012).

The Tesseract sensor (Greene et al., 2022) is a new design that takes advantage of a new racetrack core geometry to create a sensor that addresses the issues described above that are thought to cause instrumental instability in more traditional fluxgate designs which use a ring geometry core (i.e., Wallis et al., 2015; Miles et al., 2013). The Tesseract magnetometer design secures six racetrack cores within a symmetric block of 30 % glass-filled Torlon (Fig. 1a), which has a thermal coefficient of linear expansion similar to that of copper ($\sim 16\,\mathrm{ppm}\,°\mathrm{C}^{-1}$). Feedback coils are wound on the same symmetric base to reduce the tendency of the sensor's axes to skew with changes in temperature, potentially mitigating the effects of mismatched coefficients of thermal expansion which are thought to contribute to instrumental instability (Miles et al., 2017; Greene et al., 2023). These feedback coils (Fig. 1a in red) are arranged in a four-loop Merritt coil and have been optimized to generate a large region of magnetic homogeneity in the vicinity of the cores in order to improve the reproducibility of the core's magnetization, thus mitigating another potential source of instability. The sensor that was launched on ACES-II is shown in Fig. 1b. An improved flight model with lower-noise cores and opti-
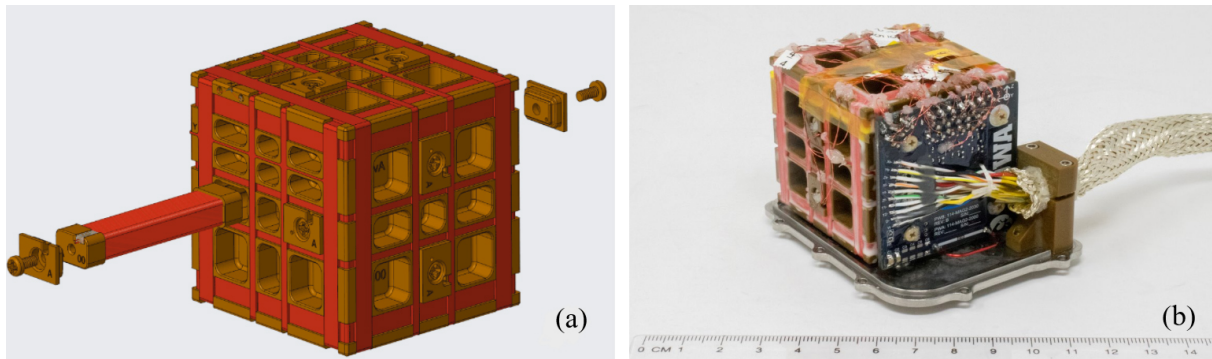
Figure 1. (a) The Tesseract magnetometer design secures six miniature low-noise racetrack cores within a symmetric block of 30 % glass-filled Torlon engineering plastic. These racetrack cores, developed by Miles et al. (2022), are wrapped in a quasi-toroidal drive winding to modulate the permeability of the core and then covered in a solenoidal sense winding to sense the modulated signal. The Tesseract's feedback coils are wound on the same glass-filled Torlon base for structural stability. These feedback coils (red) are arranged in a three-axis four-loop Merritt coil which creates a large region of magnetic homogeneity inside the sensor. **(b)** A photograph of the as-built Tesseract sensor that was flown on the ACES-II-Low sounding rocket.

mized feedback electronics is currently being prepared for the Tandem Reconnection and Cusp Electrodynamics Reconnaissance Satellites (TRACERS) mission that will launch in 2025 as part of the MAGnetometers for Innovation and Capability (MAGIC) technology demonstration.

2.1 Tesseract electronics

All the electronics are fit on a single $96 \times 91 \times 21$ mm board (Fig. 2a) which is based on the analog design from the Cassope/ePOP fluxgate (Wallis et al., 2015) and has been modified to accommodate the Tesseract sensor. Figure 2b shows the major components of a single axis of the Tesseract electronics design. A resonant drive signal (I drive) is generated by a field-programmable gate array (FPGA) and power-amplified (PA). This signal is tuned using shunt capacitance and series inductance to pulse at a frequency of $f = 8.192$ kHz (Fig. 2c) and is sent into the quasi-toroidal drive windings of all six cores in series to periodically saturate the racetrack cores. The AC current output of the sense winding (I sense) is converted to a voltage using an op-amp-based preamplifier (PRE). Figure 2d plots the voltage from the preamplifier when various background magnetic fields from $-60\,000$ to $60\,000$ nT are applied to the sensor. The signal is then bandpass-filtered in several stages (BP). The bandpass (plotted in Fig. 2e) helps block the transformer coupled $1f$ and $3f$ drive signal and minimizes aliasing during digitization.

This filtered signal then goes through a demodulation circuit (PSI) that inverts every half-period of the $2f$ signal to demodulate the fluxgate action while preserving polarity (Fig. 2f). This is then filtered by a low-pass filter (LPF) with a corner frequency of 50 Hz, resulting in a DC voltage that is directly proportional to the magnetic field. Finally, this voltage is digitized by a 20-bit analog-to-digital converter (ADC)

at 16 384 samples per second and is then down-sampled to 128 samples per second by the FPGA for telemetry. Housekeeping data such as sensor and board temperature are digitized using a separate analog-to-digital converter (HK ADC). Finally, the data are transmitted to the rocket through a serial data interface, where they are time-stamped.

Output of the low-pass filter (LPF) is converted into an offset current (I feedback) by a transconductance amplifier (V/I) and fed as input to a feedback control loop. This current is sent into the Tesseract sensor's feedback coils to actively drive the field inside the sensor towards zero. The transconductance amplifier is intentionally unbalanced so that the voltage-to-current conversion factor depends on resistance of the feedback coils. This dependence on coil resistance is then tuned until the temperature effects of the coil resistance and the coil geometry are equal and opposite. This reduces the effect of temperature on the stability of the instrumental sensitivity S due to the temperature coefficient of linear expansion of the sensors coils (Acuña et al., 1978; Primdahl and Jensen, 1982; Narod and Bennest, 1990).

2.2 The ACES-II-Low magnetometer payload

A prototype of the Tesseract instrument had an opportunity for a first flight demonstration on the ACES-II sounding rocket mission. ACES-II is a mission to study the auroral electrical current systems that are a key energy transport mechanism between the magnetosphere and the ionosphere, particularly the distribution of Hall and Pedersen currents in the current closure region (i.e., Baumjohann, 1982; Akari et al., 1989; Gjerlov and Hoffman, 2000) and the balance of each in a stable auroral system. This investigation was carried out using two rocket payloads. A high-flyer at an altitude of around 400 km observed the energy input from field-aligned currents above the closure region, and a low-flyer around
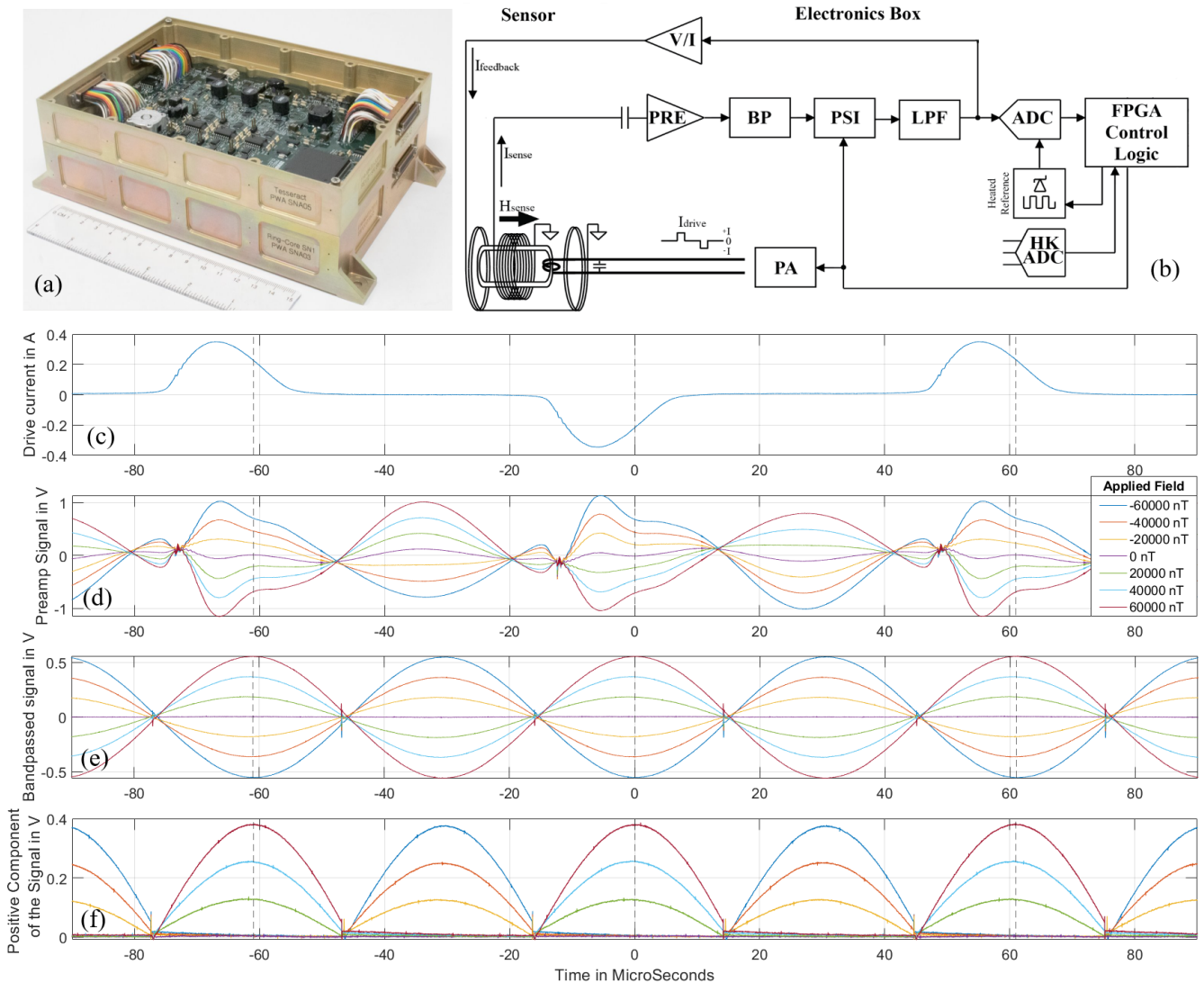
Figure 2. (a) A photograph of the electronics board which was flown on ACES-II-Low. The boards for two fluxgate instruments are stacked on top of one another. **(b)** A simplified schematic of Tesseract for a single instrument axis. **(c)** Drive pulses with a peak single-sided amplitude of about 350 mA and a frequency of 8.19 kHz are applied to the sensor's drive windings. **(d)** The output of the sense windings prior to filtering. **(e)** This signal is bandpass-filtered to remove the $2f$ transformer-coupled drive signal. The filtered signal is split into positive and negative voltage. **(f)** The negative component is inverted and added back to the positive component. Finally, this signal is low-pass-filtered, and the resulting DC voltage, which is directly proportional to the ambient magnetic field, is digitized at 128 samples per second.

the altitude of the closure current region measured the ionosphere's response to that input and the associated ionospheric energy dissipation.

Two fluxgate instruments flew on the ACES-II low-flyer sounding rocket (Fig. 3a). The prototype Tesseract sensor was mounted inboard on the low-flyer rocket mast, while a heritage ring-core sensor design (Wallis et al., 2015) was mounted outboard (Fig. 3b). The ring-core sensor's design has its heritage in the NASA MAGSAT (Acuña et al., 1978), which uses two 1″ diameter ring cores that are each wound with two orthogonal solenoidal coils, providing two measurements in the plane of each ring. The design is nearly identical to the sensors described by Miles et al. (2013) and Wallis et al. (2015). The ACES-II payload was also equipped with an electric field instrument (Bonnell et al., 2009), Langmuir probes (Keltzing et al., 1998), and ion and electron top-hat electrostatic analyzers (EEPAAs) (i.e., Carlson et al., 1982) to measure the pitch angle and energy distribution of auroral particles, as well as an electron-retarding potential analyzer (ERPA) (Cohen et al., 2016) to measure thermal electrons. The rocket was equipped with an attitude control system (ACS) which utilized a gyro to allow for spin stabilization of the rocket to about 0.6 rotations per second and post-flight determination of the attitude to less than 0.5°. It

Table 1. The characteristics of the early revision of the Tesseract fluxgate magnetometer that was flown on the ACES-II-Low sounding rocket. The temperature stability of the sensor base's sensitivity and orthogonality was characterized in a previous study and is described in Greene et al. (2022). The characterization testing procedures for noise and linearity are described in Sect. 3.

Parameter	Value
Sensor mass	343 g
Electronics mass	165 g
Sensor dimensions	$50 \times 50 \times 50$ mm
Electronics dimensions	$96 \times 91 \times 21$ mm
Power consumption	3000 mW
Sample rate	128 sps
Magnetic range	$\pm 65\,000$ nT
Linearity from $\pm 65\,000$ nT[a]	3 nT rms
Sensitivity over temperature[b]	13–17 ppm $°C^{-1}$
Orthogonality over temperature[b]	$< 0.015°$
Noise floor at 1 Hz	15–21 nT $(Hz)^{(-1/2)}$

[a] After corrections in Sect. 3.2 have been applied. [b] Between -45 and $20\,°C$ (from Greene et al., 2022).

was also equipped with an onboard Global Positioning System (GPS), which was used to acquire trajectory information.

3 Pre-flight characterization

A series of tests were conducted on the Tesseract magnetometer to quantify its performance prior to flight. The instrumental noise floor, sensitivity, orthogonality, offsets, and linearity were characterized at the University of Iowa magnetometer calibration facility and again after integration with the rocket payload at Wallops Space Flight Facility (Fig. 3c). The instrumental noise floor was also tested using a three-layered single-axis shield facility at the University of Iowa. These pre-flight test data were used to assist with the calibration and de-spin of the in situ data taken by Tesseract on ACES-II, which are described in Sect. 4.1. Table 1 shows the characteristics of the Tesseract instrument which flew on ACES-II.

The temperature stability of the Tesseract sensor's base and feedback coils, without any dependence on cores and electronics, was characterized in a previous study (Greene et al., 2022). A full thermal calibration of the entire Tesseract instrument is not explored in this paper. The sensor temperature changed by only $4\,°C$ over the course of the flight aboard ACES-II, so the errors in calibration introduced from changes in temperature are expected to be minimal. A complete temperature calibration of the Tesseract instrument which includes the cores and electronics will be performed in preparation for the upcoming TRACERS SMEX satellite mission.

Table 2. The calibration parameters for the Tesseract magnetometer on the ACES-II sounding rocket. The four calibration parameters S, A, O, and R from Eq. (1) are obtained from the pre-flight calibration testing. The rocket offset is fitted in situ against a geomagnetic field model to account for the stray magnetic field of the rocket payload.

| Calibration parameters	X	Y	Z
Sensitivity	0.0119 nT per bit	0.0145 nT per bit	0.0098 nT per bit
Orthogonality	$0.0164°$	$0.0237°$	$0.0396°$
Offset	-162 nT	142 nT	219 nT
Rotation	$0.14°$	$0.22°$	$0.49°$

3.1 Pre-flight calibration

In each pre-flight calibration measurement, the Tesseract sensor was placed inside a large three-axis coil system. The coil system was used to generate a known ambient vector magnetic field B_{Applied} of constant magnitude, which changed direction over time such that it sweeps out all solid angles of a sphere once every 5 min. The vector magnetic field measured by Tesseract B_{Measured} was recorded over the course of this test. These data were used to calibrate the Tesseract magnetometer using a method described in detail by Olsen et al. (2003) and Broadfoot et al. (2022), which exploits the relationship in Eq. (1) to fit the instrument's intrinsic calibrations parameters – orthogonality A, sensitivity S, and offset O – such that the vector residuals between the known vector field B_{Applied} and measured vector field B_{Measured} are minimized.

$$B_{\text{Applied}} = \mathbf{R}^{-1}\mathbf{A}^{-1}\mathbf{S}^{-1}(B_{\text{Measured}} - O) \qquad (1)$$

A is a 3×3 matrix that describes the projection of the magnetometer's three axes from a non-orthogonal frame onto an orthogonal frame (defined in Olsen et al., 2003). $\mathbf{S}$ is a diagonal matrix with each diagonal element representing a scale value or sensitivity that converts voltage to nanoteslas (nT) for each axis. $\mathbf{R}$ is a 3×3 rotation matrix consisting of three Euler angles that describe a rotation from the sensor frame into the frame of the rocket ACS. Uncertainty in the measurement of the Euler angles is dependent on the ability to accurately align the ACS with the coil system during calibration. We estimate that this alignment is good for angles larger than $0.05°$, and thus the uncertainty of the pre-flight estimate of the Euler angles is $0.05°$. O is simply the zero offset in each axis in nanoteslas (nT).

An iteratively reweighted least-squares linear regression (Holland and Welsch, 1977) was used to estimate the best fit for the calibration parameters that minimizes $|B_{\text{Measured}} - B_{\text{Applied}}|$. The resulting calibration parameters for each axis are shown in Table 2. These calibration parameters were applied to the data taken over the course of the flight on ACES-II prior to the in situ de-spin and calibration which are described in Sect. 4.1.
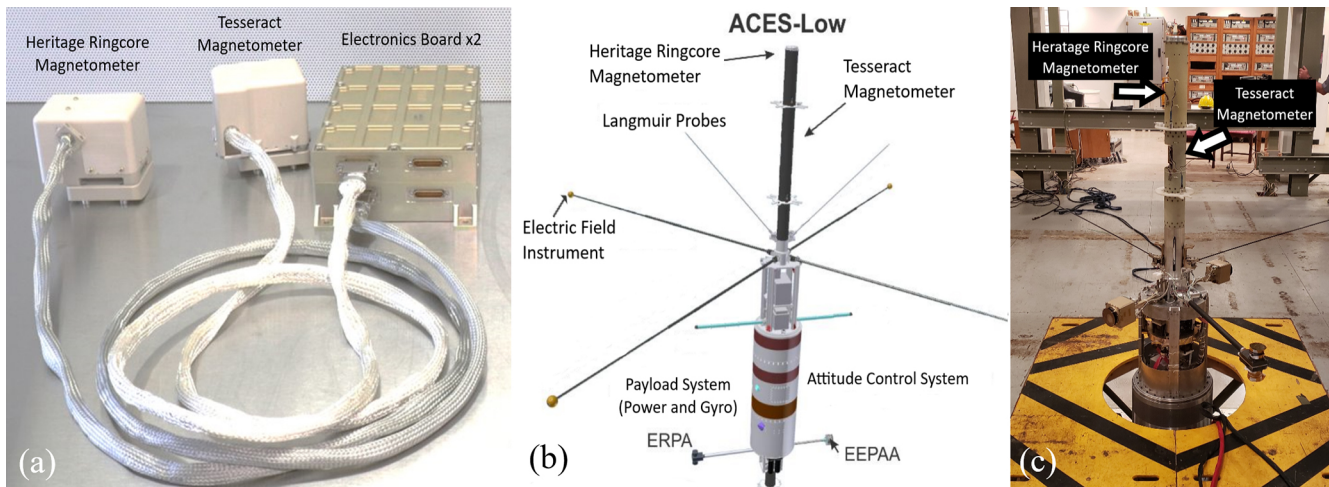
Figure 3. (a) A photograph of the magnetometer instruments which flew on ACES-II-Low. The electronics boards for each sensor are stacked on top of one another. **(b)** A diagram of the ACES-II-Low science instrument payload. The Tesseract and ring-core sensors are mounted in the rocket mast. The Tesseract is mounted inboard and the ring core is mounted outboard. **(c)** The Tesseract magnetometer and ring-core magnetometer under test at the Wallops calibration facility while mounted on the rocket.

3.2 Instrument linearity

Equation (1) assumes that the sensor's response to the applied field is linear, and thus characterization of the instrumental linearity is essential for the calibration to be effective. To characterize linearity, the coil system was used to generate a known ambient DC magnetic field. This field was ramped from $-60\,000$ to $60\,000$ nT in a series of 4000 nT steps, and the field measured by the Tesseract magnetometer was recorded. Comparison of the known applied field with the measured field allowed us to characterize the instrumental linearity from $-60\,000$ to $60\,000$ nT.

The Tesseract magnetometer uses negative magnetic feedback to null the magnetic field inside the sensor and extend the region of linear sensitivity of the permalloy core (Primdahl, 1979). The efficiency of the magnetic nulling of Tesseract magnetometer prototype that was flown on ACES-II sounding rocket is lower than planned due to limitations in the development version of the feedback electronics, which were not yet fully optimized for magnetic nulling due to flight campaign schedule constraints. At the time of integration with the ACES-II payload, the X-axis feedback channel was in the process of being tweaked to maximize the magnetic feedback efficacy to extend the region of linearity to the full Earth field, and the Y and Z feedback channels had not been optimized at all; thus, we expect to see a difference in the nonlinearity profile of the axes. The residuals of a robust multilinear regression fit (MATLAB robustfit) to the field measured by the Tesseract against the known applied field are plotted in the left half of Fig. 4 for each axis.

These trends can be reliably described by a fifth-order polynomial, a fit that represents the intrinsic nonlinearity of the prototype instrument. When the polynomial fitted to the

residuals of the data taken during calibration at Iowa is subtracted from the residual of the data taken during the calibration at Wallops, the resulting difference between the two tests is ~ 3 nT rms from $-60\,000$ to $60\,000$ nT. This test was repeated three additional times at the University of Iowa magnetometer calibration facility. Measured nonlinearity from all tests agreed to within a few nanoteslas despite different testing environments, which gives us confidence that this nonlinearity shown in Fig. 4 is highly reproducible and can be reliably corrected for in-flight. Subsequent iterations of the Tesseract's feedback electronics since the launch of ACES-II have been optimized for better linearity in preparation for a technology demonstration on the TRACERS Small Explorers satellites.
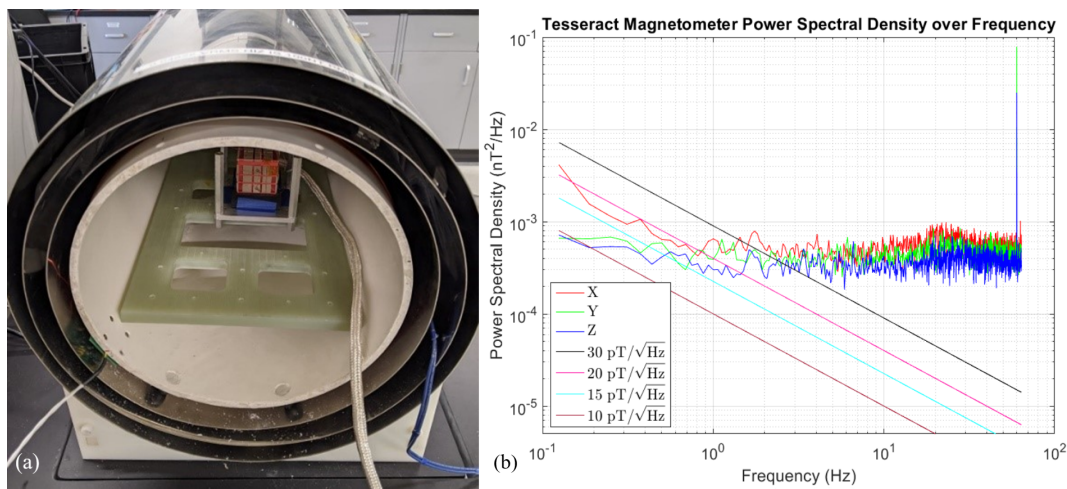
3.3 Instrumental noise

The Tesseract sensor which flew on ACES-II was made from early versions of the racetrack design (Miles et al., 2019), and the noise numbers are significantly lower in more recent fabrication efforts (i.e., Miles et al., 2022). The power spectral density noise floor of the Tesseract instrument that was flown on ACES-II was characterized prior to launch inside a single-axis three-layer Mu-metal magnetic shield (Fig. 5a).

To characterize the noise floor, 20 min of magnetically quiet data were taken while the sensor was fixed in the magnetic shield. The power spectral density of this dataset was estimated using Welch's method of overlapping periodogram segments using a Hanning window (MATLAB pwelch). The power spectral density is plotted against frequency for each axis in Fig. 5b. The spectrally narrow spike at 60 Hz is due to the ambient residual magnetic signature of the laboratory. Robust linear regression (MATLAB robustfit) was used to fit
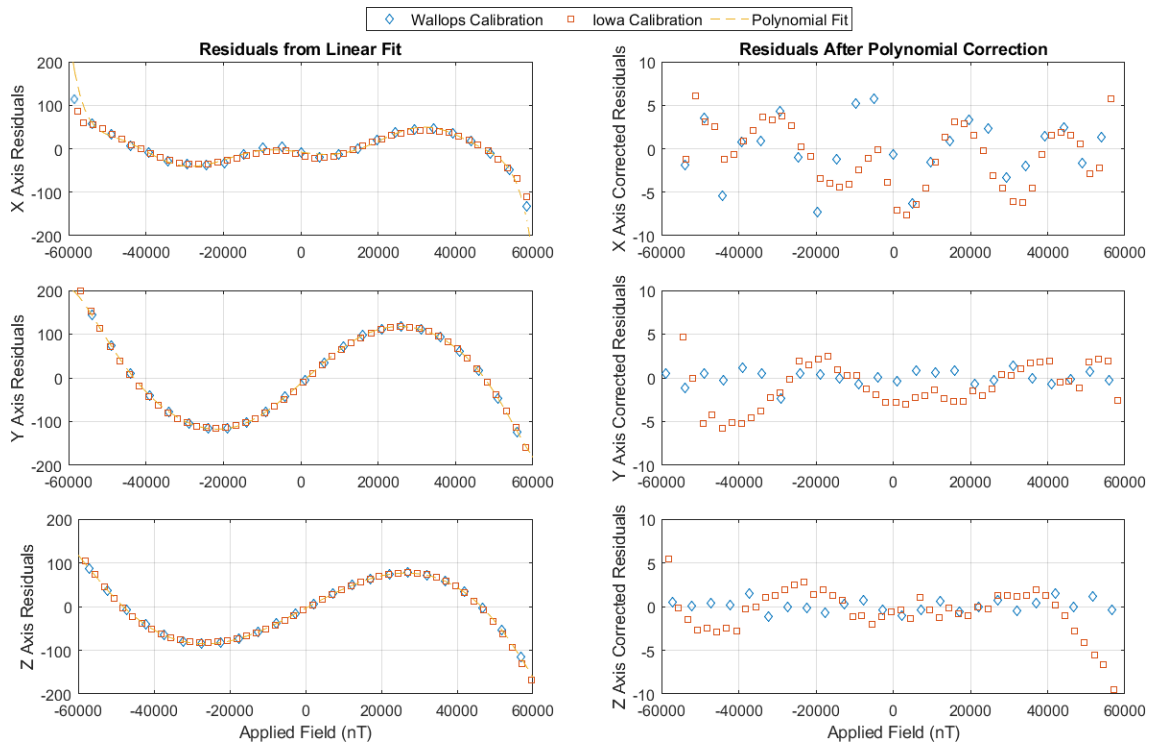
Figure 4. The residuals of a linear fit to the magnetic field measured by the Tesseract over the known applied field are plotted for each axis on the right-hand side. The residuals for the data taken using the Iowa calibration facility are plotted in red squares, while the residuals for the same test using the Wallops calibration coils are plotted in blue diamonds. The polynomial fitted to the residuals is used to correct the flight data shown in yellow. The three agree to within 3 nT rms over full magnetic range in each axis.

Figure 5. (a) Tesseract's noise floor was characterized in a three-layer Mu-metal magnetic shield. **(b)** The power spectral density of the instrumental noise plotted over frequency. The noise floor of the instrument ranges from 21 to 15 nT (Hz)$^{(-1/2)}$ at 1 Hz for each of the three axes.

a linear trend from 0.05 to 1.0 Hz, and the noise floor was evaluated at 1 Hz. The noise floor for each axis was found to be 21 nT (Hz)$^{(-1/2)}$ at 1 Hz for the X axis, 19 nT (Hz)$^{(-1/2)}$ at 1 Hz for the Y axis, and 15 nT (Hz)$^{(-1/2)}$ at 1 Hz for the Z axis.

4 In-flight performance

The Tesseract magnetometer flew on the ACES-II low-flyer: a two-stage Black Brant XI rocket which reached apogee at an altitude of 188 km. The ACES-II-Low sound-

ing rocket was launched northward from the Andøya Space Rocket Range in Andenes, Norway, on 20 November 2022 at 17:21:40 UTC into an active auroral arc. The Tesseract magnetometer took measurements of the ambient magnetic field over the course of the flight from launch until 17:28:13 UTC when connection to the rocket was lost upon re-entry. The data were calibrated in post-processing against a reference geomagnetic field model during a magnetically quiet segment of data. The Tesseract magnetometer's flight performance was evaluated via comparison to the heritage ring-core magnetometer and to the reference geomagnetic field mode. Detailed science analysis of the data will follow in a subsequent publication. The preliminary results shown here are to demonstrate instrument function.

4.1 Flight calibration and de-spin

Data taken by the Tesseract magnetometer over the course of the flight were de-spun and calibrated using a geomagnetic field model as a reference. First, the polynomials that describe the pre-flight linearity, shown in Fig. 4, were applied to each data point to correct for instrumental nonlinearity. Then the rotation matrix ($\mathbf{R}$) from the pre-flight characterization was applied to rotate the sensor body frame of the instrument into the frame of the rocket ACS. The altitude, latitude, and longitude measured by the Rocket GPS were used to evaluate the model vector field predicted by the CHAOS-7 magnetic field model (Finlay et al., 2020) at every point over the course of the flight. The attitude solution was then used to rotate the CHAOS-7 model vector field into the spinning frame of the rocket for direct comparison with the data.

Once the measured vector magnetic field and the model vector field were in the same rocket body frame, the intrinsic calibration parameters S, A, and O, obtained from pre-flight testing (Table 2), were applied to the field vector measured by Tesseract using Eq. (1) to get the data in units of nanoteslas (nT). Then an offset was fitted (rocket offset in Table 2) to the CHAOS-7 model field in all three axes during a quiet segment of data immediately before the science region (17:24:00 to 17:24:30 UTC). We attribute this offset to the stray fields of the rocket motors below the payload section that were not present during pre-flight calibrations. The background model field was subtracted from the measured magnetic field in the spinning rocket frame. Finally, the attitude data from the ACS were used to rotate the data from the spinning rocket frame into an east–north–up geophysical coordinate system.

4.2 Comparison with reference ring-core magnetometer and geomagnetic field model

The same process described above was used to de-spin and calibrate the heritage ring-core geometry sensor, which uses the same design described in Miles et al. (2013). Once calibrated and rotated into the same geophysical coordinate sys-

tem, the fields measured by the Tesseract fluxgate and the heritage ring-core science magnetometer could be directly compared. Figure 6 plots the field measured by Tesseract around the time of apogee of the rocket trajectory in red in the eastward (Fig. 6a), northward (Fig. 6b), and upward (Fig. 6) directions as well as the magnitude (Fig. 6d). The field measured by the ring-core sensor in each direction is plotted in blue.

The difference of the field measured by the two sensors is plotted in Fig. 7. Tesseract exhibits good agreement with the heritage ring-core magnetometer to within 1.91 nT rms in the eastward direction (Fig. 7a), 3.08 nT rms in the northward direction (Fig. 7b), 5.48 nT rms in the upward direction (Fig. 7c), and 0.62 nT in magnitude (Fig. 7d) over this time range. The Tesseract and ring core measured the same field in the region of auroral activity (bounded by dashed green lines in figure) to within 5.53 nT rms in all three axes. These discrepancies and remaining periodicity are due to residual spin tones introduced by small ($> 0.05°$) uncertainties in the alignment between the sensor coordinate system and the ACS coordinate system that were not accounted for in the pre-flight calibration. The pre-flight calibration procedure described in Sect. 3.1 was only able to measure Euler angles larger than $0.05°$. The uncertainty in the pre-flight characterization of the Euler angles reduces the ability to effectivity remove the effects of the rocket's spin through Earth's magnetic field, leading to a residual spin tone between the two sensors (Fig. 7).

The longitude, latitude, and altitude from the attitude data were fed as inputs into the CHAOS-7 geomagnetic field model and were used to model the geomagnetic field in the eastward, northward, and upward directions. The measured field and the model field agree to within about 25 nT rms in each axis except from 17:24:40 to 17:26:3 UTC, which corresponds to the time that the ACES-II payload traversed an auroral arc based on comparison between rocket GPS data and the data from an all-sky imager taken in Skiboten, Norway (Fig. 8). In the region associated with the auroral arc the measured field and model field agree within 37 nT rms in each axis. We take this agreement with the science magnetometer and the CHAOS-7 magnetic field model as validation that the Tesseract instrument functioned as expected.

5 Measurement of magnetic signatures associated with auroral currents

A map of the ACES-II low-flyer trajectory measured by the ACS GPS is shown in Fig. 7 plotted on top of an all-sky image of 630 nm wavelength light taken at the Tromsø Geophysical Observatory in Skiboten, Norway, at 17:25:00 UTC, which has been projected onto the corresponding longitude and latitude. Based on the trajectory of all-sky imager data, ACES-II is expected to have traversed at least one active auroral arc between 17:24:40 and 17:26:30 UTC. The visi-
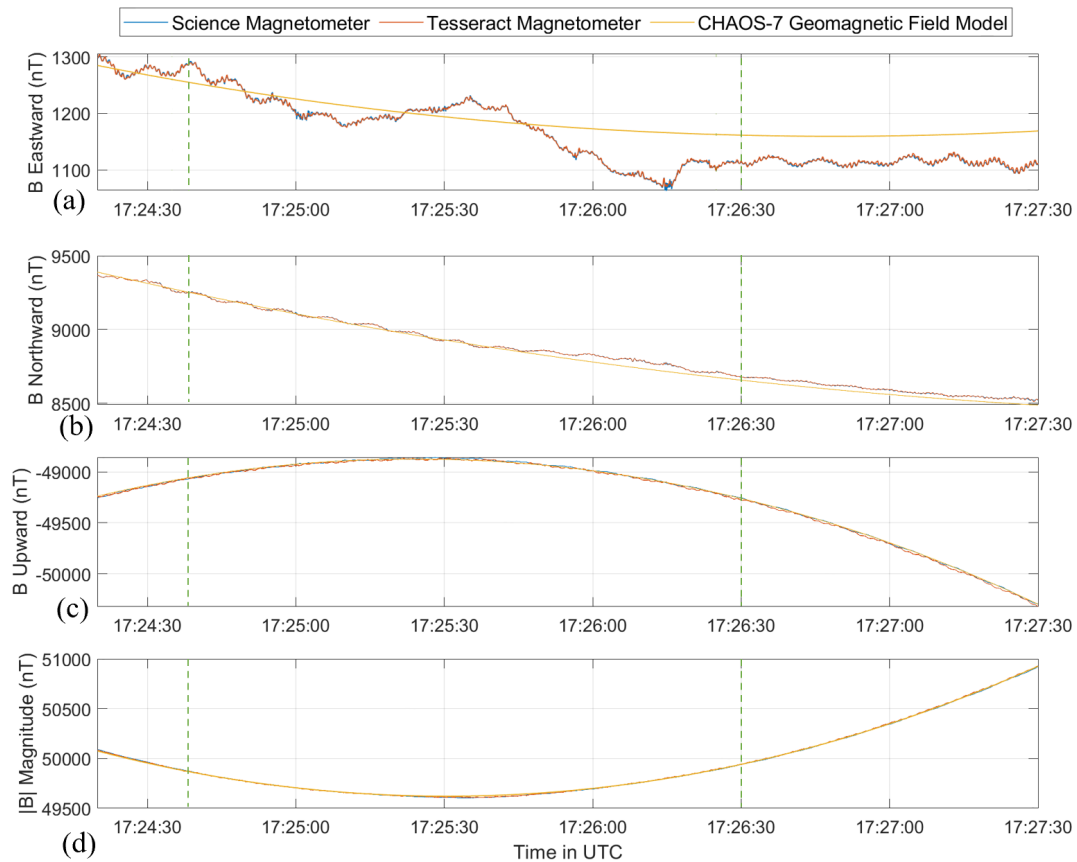
Figure 6. During a quiet segment of data, between 17:24:00 and 17:24:30 UTC, the ring-core and Tesseract data were calibrated using the calibration values obtained during pre-flight testing. The magnetic field measured by the Tesseract magnetometer is plotted over time in red, and the measured field by the ring core is plotted in blue for the eastward **(a)**, northward **(b)**, and upward **(c)** directions. The scalar magnetic field is plotted in **(d)**. The magnetic field predicted by the CHAOS-7 geomagnetic field model was evaluated at the rocket's location over the course of the flight and is plotted in yellow. The region where we expect to observe auroral activity based on the all-sky image is bounded by dotted green lines.

ble auroral arc remained relatively stable over the course of the flight but slowly drifted equatorward. However, at about 17:20:35 UTC, 8 min after the flight ended, a surge drove the visible arc southward, and it quickly evolved into a dynamic auroral substorm. The arc was on the horizon, so any fine structure would have been obscured.

The deviation of the magnetic field measured by Tesseract from the background model field over the course of the flight is plotted in red. The measured field deviates from the nominal magnetic field from 17:24:40–17:26:30 UTC by a maximum of about 50 nT in the east direction, 25 nT in the north direction, and 15 nT in the up direction. This time range corresponds to the time that the ACES-II payload traversed an auroral arc based on data from an all-sky imager (Fig. 8). The magnetic field is in the eastward direction, implying that these magnetic fluctuations are primarily measurements of the east–west field-aligned current sheet that is likely associated with the aurora.

Figure 9a plots one of the transverse components of the magnetic field (eastward) measured by Tesseract, which has been computationally high-pass-filtered over 1 Hz using a simple running mean filter (MATLAB highpass) to suppress the background magnetic field. This crudely filters out the residual spin tone, leaving just the higher-frequency fluctuations to highlight the AC magnetic field (Fig. 9a). The spectrogram of these data, plotted in Fig. 8b shows, mostly broadband magnetic fluctuations from about 1–8 Hz.

The magnetic perturbations encountered from 17:24:40 to 17:26:30 UTC (marked by dotted green lines) could potentially be signatures of Alfvén waves, which are responsible for transferring energy between the magnetosphere and ionosphere. Alfvén waves with broadband frequencies up to 8 Hz are often observed in conjunction with the discrete aurora (Stasiewicz et al., 2000, and the references therein) and can be responsible for accelerating electrons that power the aurora (Schroeder et al., 2021; Kletzing, 1994; Chaston et al., 2007). Alfvén waves are also thought to play a role in driving
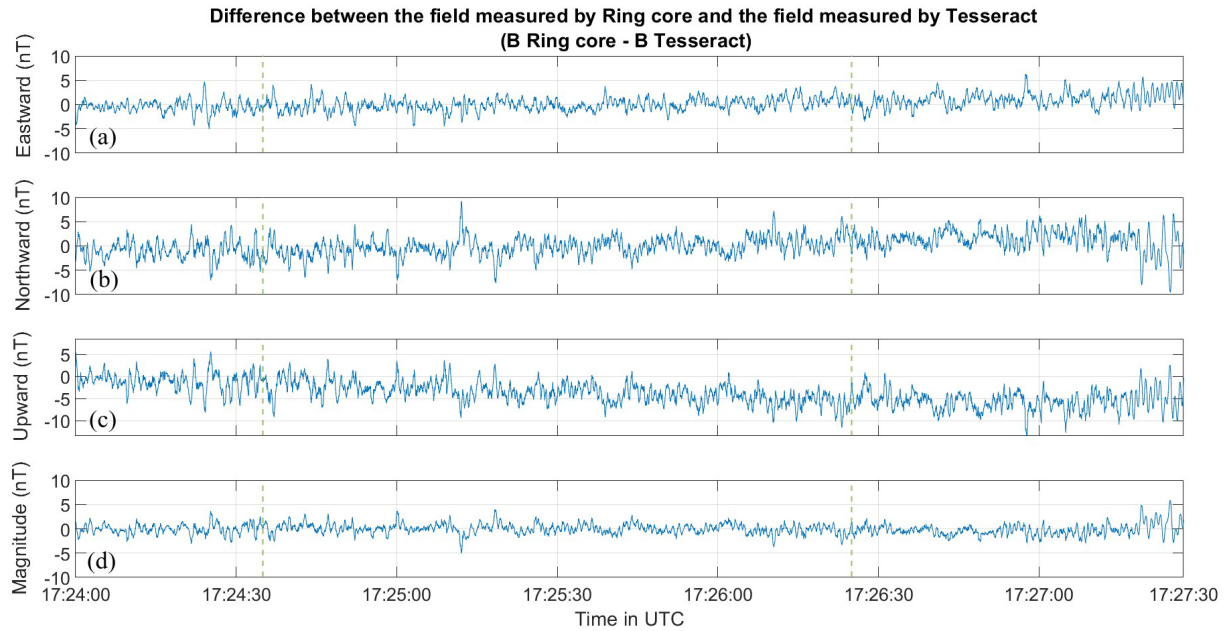
Figure 7. The difference between the magnetic field measured by the heritage ring-core science magnetometer and the magnetic field measured by the Tesseract is plotted for the eastward **(a)**, northward **(b)**, and upward **(c)** directions, along with the scalar **(d)** field. The region where the rocket payload is expected to have crossed the auroral arc is bounded by dashed green lines.
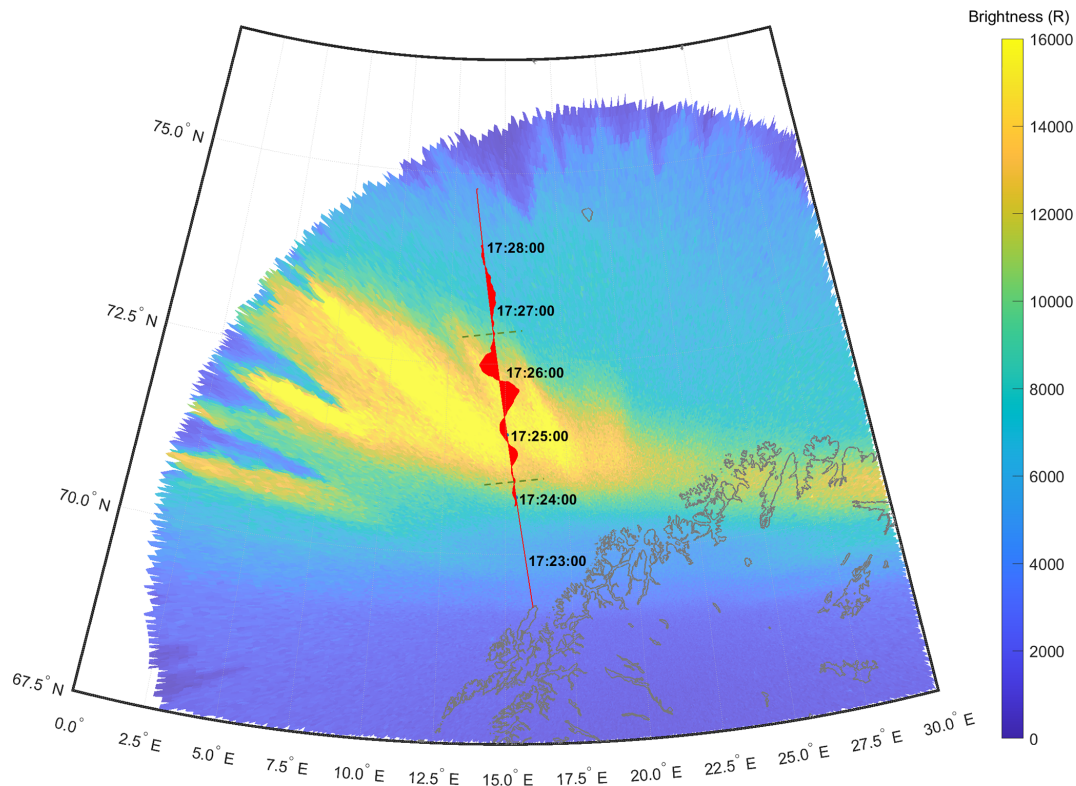
Figure 8. An all-sky image taken in Skiboten, Norway, at 17:25:30 UTC is projected onto its approximate location and is plotted alongside the trajectory of the ACES-II low-flyer as measured by the rocket GPS. The eastward DC magnetic field that Tesseract magnetometer measures over the course of the flight is plotted in red. Around the apogee, from 17:24:40 to 17:26:30 UTC, the ACES-II low-flyer passes through at least one an active auroral arc.
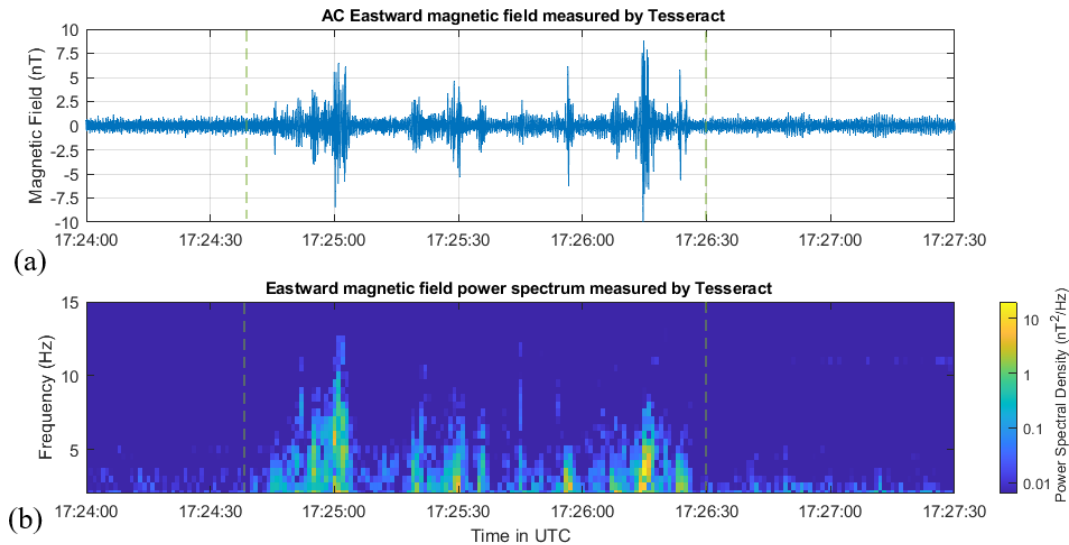
Figure 9. High-pass-filtering the data at 1 Hz removes the DC background magnetic field, allowing us to highlight the AC signature in the data. **(a)** We observe magnetic fluctuations with amplitudes up to 8 nT at the same times that the ACES-II-Low payload crosses the visible auroral arc show in Fig. 8. **(b)** The power spectrum of these data shows that these fluctuations have frequencies up to 8 Hz.

Joule heating (Hartinger et al., 2015; Chaston et al., 2006) and ion outflow (Fernandes et al., 2016) in the ionosphere. A more detailed scientific investigation using multiple instruments on ACES-II is underway and will be published separately.

6   Summary and conclusion

A new fluxgate magnetometer design is presented. The procedures and results of a full calibration and characterization of the instrument's pre-flight performance are presented. In situ performance of the instrument's first space flight was found to be in good agreement with the pre-flight calibrations, the onboard heritage science magnetometer, and the CHAOS-7 geomagnetic field model. We find that the magnetic field measured by the Tesseract magnetometer corresponded to the heritage science magnetometer to within 5.5 nT rms in all three axes and to the field predicted by the CHAOS-7 geomagnetic field model to within 25 nT rms during geomagnetically quiet times. We conclude that the Tesseract magnetometer performed as expected, and the calibration efforts were successful.

Additionally, the Tesseract magnetometer observes perturbations in the background magnetic field as large as 50 nT and AC magnetic fluctuations between 1 and 8 Hz, which are coincident with the crossing of an active auroral current sheet, suggesting that these fluctuations may be involved with transporting energy and accelerating auroral electrons and ions that couple the ionosphere to the magnetosphere. We demonstrate the capability of a new magnetometer design to measure a geophysical magnetic field in a space en-

vironment that is potentially relevant for scientific studies of auroral electrodynamics.

Future work

Once the data for the rest of the ACES-II instruments have been processed and calibrated, we will compare the data taken by Tesseract with the data taken by the onboard electric field instruments to determine whether the observed magnetic fluctuations are signatures of Alfvén waves or quasistatic currents that have been Doppler-shifted in the rocket frame (Knudsen et al., 1992). We will compare these data to the data taken with the electron and ion instruments to determine whether these fluctuations are associated with electron or ion acceleration and transport and whether they might play a role in transporting energy from the magnetosphere to the ionosphere. We will also compare this to the plasma density measurement taken with the onboard Langmuir probes, which will be used to estimate the Alfvén speed and ionospheric conductivity.

The development of the Tesseract magnetometer is ongoing. The closed-loop feedback electronics are being optimized to minimize nonlinearity on future iterations of the instrument. The Tesseract magnetometer will be flight-demonstrated again with lower-noise racetrack cores (Miles et al., 2022) and improved negative feedback electronics on the upcoming Tandem Reconnection and Cusp Electrodynamics Reconnaissance Satellites (TRACERS) Small Explorers mission (Kletzing, 2019) as part of the MAGIC technology demonstration.

References

Acuna, M. H., Scearce, C. S., Seek, J., and Scheifele, J.: The MAGSAT vector magnetometer: A precision fluxgate magnetometer for the measurement of the geomagnetic field, Technical report, National Aeronautics and Space Administration, Goddard Space Flight Center, Greenbelt, Maryland, https://ntrs.nasa.gov/citations/19790010349 (last access: 30 July 2024), 1978.

Araki, T., Schlegel, K., and Lühr, H.: Geomagnetic effects of the Hall and Pedersen current flowing in the auroral ionosphere, J. Geophys. Res., 94, 17185–17199, https://doi.org/10.1029/JA094iA12p17185, 1989.

Auster, H. U., Glassmeier, K. H., Magnes, W., Aydogar, O., Baumjohann, W., Constantinescu, D., Fischer, D., Fornacon, K. H., Georgescu, E., Harvey, P., and Hillenmaier, O.: The THEMIS Fluxgate Magnetometer, Space Sci. Rev., 141, 235–264, https://doi.org/10.1007/s11214-008-9365-9, 2008.

Balogh, A., Dunlop, M. W., Cowley, S. W. H., Southwood, D. J., Thomlinson, J. G., Glassmeier, K. H., Musmann, G., Lühr, H., Buchert, S., Acuña, M. H., Fairfield, D. H., Slavin, J. A., Riedler, W., Schwingenschuh, K., and Kivelson, M. G.: The Cluster Magnetic Field Investigation, in: The Cluster and Phoenix Missions, edited by: Escoubet, C. P., Russell, C. T., and Schmidt, R., Springer Netherlands, Dordrecht, 65–91, https://doi.org/10.1007/978-94-011-5666-0_3, 1997.

Baumjohann, W.: Ionospheric and field-aligned current systems in the auroral zone: a concise review, Adv. Space Res., 2, 55–62, https://doi.org/10.1016/0273-1177(82)90363-5, 1982.

Bonnell, J. W., Mozer, F. S., Delory, G. T., Hull, A. J., Ergun, R. E., Cully, C. M., Angelopoulos, V., and Harvey, P. R.: The Electric Field Instrument (EFI) for THEMIS, in: The THEMIS Mission, edited by: Burch, J. L. and Angelopoulos, V., Springer, New York, NY, 303–341, https://doi.org/10.1007/978-0-387-89820-9_14, 2009.

Broadfoot, R. M., Miles, D. M., Holley, W., and Howarth, A. D.: In situ calibration of the Swarm-Echo magnetometers, Geosci. Instrum. Method. Data Syst., 11, 323–333, https://doi.org/10.5194/gi-11-323-2022, 2022.

Carlson, C. W., Curtis, D. W., Paschmann, G., and Michel, W.: An instrument for rapidly measuring plasma distribution functions with high resolution, Adv. Space Res., 2, 67–70, https://doi.org/10.1016/0273-1177(82)90151-X, 1982.

Chasapis, A., Matthaeus, W. H., Bandyopadhyay, R., Chhiber, R., Ahmadi, N., Ergun, R. E., Russell, C. T., Strangeway, R. J., Giles, B. L., Gershman, D. J., Pollock, C. J., and Burch, J. L.: Scaling and Anisotropy of Solar Wind Turbulence at Kinetic Scales during the MMS Turbulence Campaign, Astrophys. J., 903, 127–138, https://doi.org/10.3847/1538-4357/abb948, 2020.

Geosci. Instrum. Method. Data Syst., 13, 249–262, 2024

https://doi.org/10.5194/gi-13-249-2024

Chaston, C. C., Genot, V., Bonnell, J. W., Carlson, C. W., McFadden, J. P., Ergun, R. E., Strangeway, R. J., Lund, E. J., and Hwang, K. J.: Ionospheric erosion by Alfvén waves, J. Geophys. Res., 111, 2005JA011367, https://doi.org/10.1029/2005JA011367, 2006.

Chaston, C. C., Carlson, C. W., McFadden, J. P., Ergun, R. E., and Strangeway, R. J.: How important are dispersive Alfvén waves for auroral particle acceleration?, Geophys. Res. Lett., 34, 2006GL029144, https://doi.org/10.1029/2006GL029144, 2007.

Cheng, Z. W., Shi, J. K., Torkar, K., Lu, G. P., Dunlop, M. W., Carr, C. M., Rème, H., Dandouras, I., and Fazakerley, A.: Impact of the Solar Wind Dynamic Pressure on the Field-Aligned Currents in the Magnetotail: Cluster Observation, J. Geophys. Res.-Space, 126, e2021JA029785, https://doi.org/10.1029/2021JA029785, 2021.

Chhiber, R., Chasapis, A., Bandyopadhyay, R., Parashar, T. N., Matthaeus, W. H., Maruca, B. A., Moore, T. E., Burch, J. L., Torbert, R. B., Russell, C. T., Le Contel, O., Argall, M. R., Fischer, D., Mirioni, L., Strangeway, R. J., Pollock, C. J., Giles, B. L., and Gershman, D. J.: Higher-Order Turbulence Statistics in the Earth's Magnetosheath and the Solar Wind Using Magnetospheric Multiscale Observations, J. Geophys. Res.-Space, 123, 9941–9954, https://doi.org/10.1029/2018JA025768, 2018.

Cohen, I. J., Widholm, M., Lessard, M. R., Riley, P., Heavisides, J., Moen, J. I., Clausen, L. B. N., and Bekkeng, T. A.: Rocket-borne measurements of electron temperature and density with the Electron Retarding Potential Analyzer instrument, J. Gepophys. Res.-Space, 121, 6774–6782, https://doi.org/10.1002/2016JA022562, 2016.

Finlay, C. C., Kloss, C., Olsen, N., Hammer, M. D., Tøffner-Clausen, L., Grayver, A., and Kuvshinov, A.: The CHAOS-7 geomagnetic field model and observed changes in the South Atlantic Anomaly, Earth Planets Space, 72, 156–187, https://doi.org/10.1186/s40623-020-01252-9, 2020.

Fernandes, P. A., Lynch, K. A., Zettergren, M., Hampton, D. L., Bekkeng, T. A., Cohen, I. J., Conde, M., Fisher, L. E., Horak, P., Lessard, M. R., Miceli, R. J., Michell, R. G., Moen, J., and Powell, S. P.: Measuring the seeds of ion outflow: Auroral sounding rocket observations of low-altitude ion heating and circulation, J. Geophys. Res.-Space, 121, 1587–1607, https://doi.org/10.1002/2015JA021536, 2016.

Gjerloev, J. W. and Hoffman, R. A.: Height-integrated conductivity in auroral substorms: 2. Modeling, J. Geophys. Res., 105, 227–235, https://doi.org/10.1029/1999JA900353, 2000.

Gjerloev, J. W., Ohtani, S., Iijima, T., Anderson, B., Slavin, J., and Le, G.: Characteristics of the terrestrial field-aligned current system, Ann. Geophys., 29, 1713–1729, https://doi.org/10.5194/angeo-29-1713-2011, 2011.

Greene, K., Hansen, C., Narod, B. B., Dvorsky, R., and Miles, D. M.: Tesseract – a high-stability, low-noise fluxgate sensor designed for constellation applications, Geosci. Instrum. Method. Data Syst., 11, 307–321, https://doi.org/10.5194/gi-11-307-2022, 2022.

Greene, K., Hansen, C. T., and Miles, D. M.: On the Impact of Thermal Gradients Across Fluxgate Sensors on In Situ Magnetic Field Measurements, J. Geophys. Res.-Space, 128, e2023JA031369, https://doi.org/10.1029/2023JA031369, 2023.

Hartinger, M. D., Moldwin, M. B., Zou, S., Bonnell, J. W., and Angelopoulos, V.: ULF wave electromagnetic energy flux into the ionosphere: Joule heating implications, J. Geophys. Res.-Space, 120, 494–510, https://doi.org/10.1002/2014JA020129, 2015.

Holland, P. W. and Welsch, R. E.: Robust regression using iteratively reweighted least-squares, Commun. Stat., 6, 813–827, https://doi.org/10.1080/03610927708827533, 1977.

Kletzing, C.: The Tandem Reconnection And Cusp Electrodynamics Reconnaissance Satellites (TRACERS) Mission, in: vol. 2019, AGU Fall Meeting Abstracts, 19 December 2019, San Francisco, CA, USA, A41U-2687, 2019.

Kletzing, C. A.: Electron acceleration by kinetic Alfvén waves, J. Geophys. Res., 99, 11095–11103, https://doi.org/10.1029/94JA00345, 1994.

Kletzing, C. A., Mozer, F. S., and Torbert, R. B.: Electron temperature and density at high latitude, J. Geophys. Res., 103, 14837–14845, https://doi.org/10.1029/98JA00962, 1998.

Knudsen, D. J., Kelley, M. C., and Vickrey, J. F.: Alfvén waves in the auroral ionosphere: A numerical model compared with measurements, J. Geophys. Res., 97, 77–90, https://doi.org/10.1029/91JA02300, 1992.

Korepanov, V. and Marusenkov, A.: Flux-Gate Magnetometers Design Peculiarities, Surv. Geophys., 33, 1059–1079, https://doi.org/10.1007/s10712-012-9197-8, 2012.

Lühr, H., Park, J., Gjerloev, J. W., Rauberg, J., Michaelis, I., Merayo, J. M. G., and Brauer, P.: Field-aligned currents' scale analysis performed with the Swarm constellation, Geophys. Res. Lett., 42, 1–8, https://doi.org/10.1002/2014GL062453, 2015.

Merayo, J. É. M. G., Jørgensen, J. L., Friis-Christensen, E., Brauer, P., Primdahl, F., Jørgensen, P. S., Allin, T. H., and Denver, T.: The Swarm Magnetometry Package, in: Small Satellites for Earth Observation, edited by: Sandau, R., Röser, H.-P., and Valenzuela, A., Springer Netherlands, Dordrecht, 143–151, https://doi.org/10.1007/978-1-4020-6943-7_13, 2008.

Miles, D. M., Bennest, J. R., Mann, I. R., and Millling, D. K.: A radiation hardened digital fluxgate magnetometer for space applications, Geosci. Instrum. Method. Data Syst., 2, 213–224, https://doi.org/10.5194/gi-2-213-2013, 2013.

Miles, D. M., Mann, I. R., Kale, A., Milling, D. K., Narod, B. B., Bennest, J. R., Barona, D., and Unsworth, M. J.: The effect of winding and core support material on the thermal gain dependence of a fluxgate magnetometer sensor, Geosci. Instrum. Method. Data Syst., 6, 377–396, https://doi.org/10.5194/gi-6-377-2017, 2017.

Miles, D. M., Ciurzynski, M., Barona, D., Narod, B. B., Bennest, J. R., Kale, A., Lessard, M., Milling, D. K., Larson, J., and Mann, I. R.: Low-noise permalloy ring cores for fluxgate magnetometers, Geosci. Instrum. Method. Data Syst., 8, 227–240, https://doi.org/10.5194/gi-8-227-2019, 2019.

Miles, D. M., Dvorsky, R., Greene, K., Hansen, C. T., Narod, B. B., and Webb, M. D.: Contributors to fluxgate magnetic noise in permalloy foils including a potential new copper alloy regime, Geosci. Instrum. Method. Data Syst., 11, 111–126, https://doi.org/10.5194/gi-11-111-2022, 2022.

Narod, B. B. and Bennest, J. R.: Ring-core fluxgate magnetometers for use as observatory variometers, Phys. Earth Planet. Inter., 59, 23–28, https://doi.org/10.1016/0031-9201(90)90205-C, 1990.

Narod, B. B. and Miles, D. M.: Copper permalloys for fluxgate magnetometer sensors, Geosci. Instrum. Method. Data Syst., 13, 131–161, https://doi.org/10.5194/gi-13-131-2024, 2024.

Olsen, N., Tøffner-Clausen, L., Sabaka, T. J., Brauer, P., Merayo, J. M. G., Jørgensen, J. L., Léger, J. M., Nielsen, O. V., Primdahl, F., and Risbo, T.: Calibration of the Ørsted vector magnetometer, Earth Planets Space, 55, 11–18, https://doi.org/10.1186/BF03352458, 2003.

Pakhotin, I. P., Mann, I. R., Knudsen, D. J., Lysak, R. L., and Burchill, J. K.: Diagnosing the Role of Alfvén Waves in Global Field-Aligned Current System Dynamics During Southward IMF: Swarm Observations, J. Geophys. Res.-Space, 125, e2019JA027277, https://doi.org/10.1029/2019JA027277, 2020.

Primdahl, F.: The fluxgate magnetometer, J. Phys. E, 12, 241–253, https://doi.org/10.1088/0022-3735/12/4/001, 1979.

Schroeder, J. W. R., Howes, G. G., Kletzing, C. A., Skiff, F., Carter, T. A., Vincena, S., and Dorfman, S.: Laboratory measurements of the physics of auroral electron acceleration by Alfvén waves, Nat. Commun., 12, 3103, https://doi.org/10.1038/s41467-021-23377-5, 2021.

Stasiewicz, K., Bellan, P., Chaston, C., Kletzing, C., Lysak, R., Maggs, J., Pokhotelov, O., Seyler, C., Shukla, P., Stenflo, L., Streltsov, A., and Wahlund, J.-E.: Small Scale Alfvenic Structure in the Aurora, Space Sci. Rev., 92, 423–533, https://doi.org/10.1023/A:1005207202143, 2000.

Petrucha, V., Janosek, M., and Azpurua, M. A.: Vector Feedback Homogeneity and Inner Layout Influence on Fluxgate Sensor Parameters, IEEE T. Instrum. Meas., 64, 1285–1291, https://doi.org/10.1109/TIM.2014.2362831, 2015.

Primdahl, F.: The fluxgate magnetometer, J. Phys. E, 12, 241–253, https://doi.org/10.1088/0022-3735/12/4/001, 1979.

Primdahl, F. and Jensen, P. A.: Compact spherical coil for fluxgate magnetometer vector feedback, J. Phys. E, 15, 221–226, https://doi.org/10.1088/0022-3735/15/2/015, 1982.

Ripka, P.: Advances in Fluxgate Sensors, Sensors Actuat. A, 106, 8–14, https://doi.org/10.1016/S0924-4247(03)00094-3, 1992.

Russell, C. T., Anderson, B. J., Baumjohann, W., Bromund, K. R., Dearborn, D., Fischer, D., Le, G., Leinweber, H. K., Leneman, D., Magnes, W., and Means, J. D.: The Magnetospheric Multiscale Magnetometers, Space Sci. Rev., 199, 189–256, https://doi.org/10.1007/s11214-014-0057-3, 2016.

Slavin, J. A., Le, G., Strangeway, R. J., Wang, Y., Boardsen, S. A., Moldwin, M. B., and Spence, H. E.: Space Technology 5 Multi-Point Measurements of near-Earth Magnetic Fields: Initial Results, Geophys. Res. Lett., 35, L02107, https://doi.org/10.1029/2007GL031728, 2008.

Wallis, D. D., Miles, D. M., Narod, B. B., Bennest, J. R., Murphy, K. R., Mann, I. R., and Yau, A. W.: The CASSIOPE/e-POP Magnetic Field Instrument (MGF), Space Sci. Rev., 189, 27–39, https://doi.org/10.1007/s11214-014-0105-z, 2015.